nature communications

Article

https://doi.org/10.1038/s41467-024-53369-0

Vapor kinetic energy for the detection and understanding of atmospheric rivers

Received: 5 December 2022

Accepted: 10 October 2024

Published online: 04 November 2024

Check for updates

Hing Ong[1] & Da Yang[2]

Poleward water vapor transport in the midlatitudes mainly occurs in meandering filaments of intense water vapor transport, spanning thousands of kilometers long and hundreds of kilometers wide and moving eastward. The water vapor filaments are known as atmospheric rivers (ARs). They can cause extreme wind gusts, intense precipitation, and flooding along densely populated coastal regions. Many recent studies about ARs focused on the statistical analyses of ARs, but a process-level understanding of ARs remains elusive. Here we show that ARs are streams of air with enhanced vapor kinetic energy (VKE) and derive a governing equation for Integrated VKE to understand what contributes to the evolution of ARs. We find that ARs grow mainly because of potential energy conversion to kinetic energy, decay largely owing to condensation and turbulence, and the eastward movement is primarily due to horizontal advection of VKE. Our VKE framework complements the integrated vapor transport framework, which is popular for identifying ARs but lacks a prognostic equation for understanding the physical processes.

An atmospheric river (AR) is a narrow corridor of water vapor transported by strong winds at low altitudes—a low-level jet[1]. ARs often form with the development of extratropical cyclones and their associated cold fronts[1–3] and move eastward. On average, each AR transports more water than the flow of the Amazon River[4,5]. ARs contribute most of the poleward water vapor transport in the midlatitudes[5,6] and can lead to extreme winds[7] and precipitation in coastal regions around the world[7–13]. For example, in October 2021, an atmospheric river made landfall in California and brought strong winds with peak gusts around 70 mph and historic heavy rainfall, leading to flooding, power outages, and mud slides[14]. ARs' impact on hydrological cycle has aroused growing research interest in the past decade[15]. The scientific community has collaborated to detect ARs and quantify their statistical features, including frequency, intensity, duration, etc. in the AR Tracking Method Intercomparison Project (ARTMIP)[6,16,17]. However, it remains unclear what physical process provide energy to maintain ARs, and what physical processes lead to the eastward movement of ARs.

Since ARs are associated with both high humidity and strong winds, ARs are often detected using integrated vapor transport (IVT)[6]:

$$\mathrm{IVT} \equiv \sqrt{\left(-\frac{1}{g}\int_{p_\mathrm{B}}^{p_\mathrm{T}} qu\mathrm{d}p\right)^2 + \left(-\frac{1}{g}\int_{p_\mathrm{B}}^{p_\mathrm{T}} qv\mathrm{d}p\right)^2}, \quad (1)$$

where the variables are defined as follows: q, specific humidity; u, zonal velocity; v, meridional velocity; g, gravity; and p, pressure. The lower limit, p_B, is surface pressure. The upper limit, p_T, is a constant pressure beyond which specific humidity is negligible; p_T is set to 200 hPa[16]. ARs' IVT anomalies are sometimes dominated by high humidity and sometimes by strong winds[18].

Unfortunately, it is challenging to derive a budget equation or conservation law for IVT, so most previous studies analyzed the column water vapor (CWV) budget to study the evolution of ARs[19–23]. They showed that horizontal convergence is the primary source of water vapor in ARs, which is then lost through water vapor condensation and precipitation[19–22]. This result broadly agrees with a Lagrangian analysis of CWV anomalies[23]. These studies implicitly assumed that evolution of winds is of secondary importance to the physics of ARs, a compromise

[1]Argonne National Laboratory, Lemont, IL, USA. [2]University of Chicago, Chicago, IL, USA. e-mail: dayang@uchicago.edu

of lacking an analysis method that accounts for both winds and humidity. However, since the development of ARs is closely tied to the lifecycle of baroclinic waves and extratropical cyclones[1–3], and much of their impact is also attributed to intense winds[7], it is imperative to establish an analysis framework that organically incorporates both wind and humidity elements.

Here we propose using vapor kinetic energy (VKE) to study ARs. Starting from vapor transport, qu and qv, we define VKE as $[(qu)^2 + (qv)^2] / 2 = q^2K$, where K denotes kinetic energy (KE) in horizontal winds per unit mass ($[u^2 + v^2]/2$). If we consider vapor transport as specific humidity-weighted momentum, then VKE is the corresponding energy. By construction, VKE always increases with the magnitude of vapor transport. Then, we define integrated VKE (IVKE) as follows:

$$\mathrm{IVKE} \equiv -\frac{1}{g}\int_{p_B}^{p_T} q^2 K \,\mathrm{d}p. \tag{2}$$

We will show that IVKE is as effective as IVT in AR detection and that the budget of IVKE exposes the physics of ARs' evolution.

Results

We first show the IVT- and IVKE-based detection results using the TempestExtremes algorithm[24] and the Modern-Era Retrospective analysis for Research and Application, version 2 (MERRA-2) data[25]. The detection results are almost identical in terms of AR presence (Supplementary Video S1) and frequency (Fig. 1a, b). The frequency difference between IVT and IVKE is on the order of 1 day per year (Fig. 1c). Both Supplementary Video S1 and Fig. 1a, b seamlessly juxtapose the panels of results using IVT and IVKE. The results match in most details, and the transition between the results is almost continuous; the detected ARs on the right of the left panel (using IVT) appear on the left of the right panel (using IVKE) as if the right panel was an extension of the left panel. Also, the AR frequency in Fig. 1 is similar to the ensemble median of ARTMIP in terms of the spatial patterns and the maximum values[17]. We then use an independent detection algorithm developed by Mundhenk et al.[26] to further compare the IVT- and IVKE-based AR detection. The overall results remain similar: using IVKE can effectively capture AR events (Fig. 1d–f). These results suggest that ARs are streams of air with enhanced IVKE, and the evolution of IVKE may explain the evolution of ARs.

Figure 1c, f provides an opportunity to compare AR detection results based on different algorithms. The frequency difference caused by switching from the TempestExtremes algorithm to the Mundhenk et al. algorithm is approximately 10 days per year over the mid-latitudes, which is similar to the ensemble interquartile range reported by ARTMIP[17]. In contrast, the frequency difference when switching from IVT to IVKE is about 2 days per year using TempestExtremes and about 4 days per year using the Mundhenk et al. algorithm over the mid-latitudes. This indicates that switching from IVT to IVKE introduces a smaller AR frequency difference compared to the change between detection algorithms. Readers can find more detailed comparisons of AR detection algorithms in the ARTMIP reports.

We then derive a budget equation for IVKE by combining the conservation of momentum and water vapor to understand ARs' evolution (Methods). The IVKE tendency can be decomposed into two components: one component is the sum of the vertical integral of VKE tendency, and the other component is related to changes in surface pressure with time (Eqs. (9) and (10)), where the latter term is negligible in our analysis. Therefore, the key equation is the VKE tendency equation (simplified from Eq. (8)):

$$\frac{\partial q^2K}{\partial t} = -\mathbf{u}\cdot\nabla_p(q^2K) - \omega\frac{\partial q^2K}{\partial p} - q^2\mathbf{u}\cdot\nabla_p\Phi + q^2\mathbf{u}\cdot\mathbf{F_T} + 2KqS_M + \mathrm{Other}. \tag{3}$$

The right-hand side of Eq. (3) shows that the primary contributors to the evolution of VKE are horizontal advection of VKE ($-\mathbf{u}\cdot\nabla_p(q^2K)$), vertical advection of VKE ($-\omega\frac{\partial q^2K}{\partial p}$), potential energy (PE) conversion to KE ($-q^2\mathbf{u}\cdot\nabla_p\Phi$), turbulent dissipation of KE

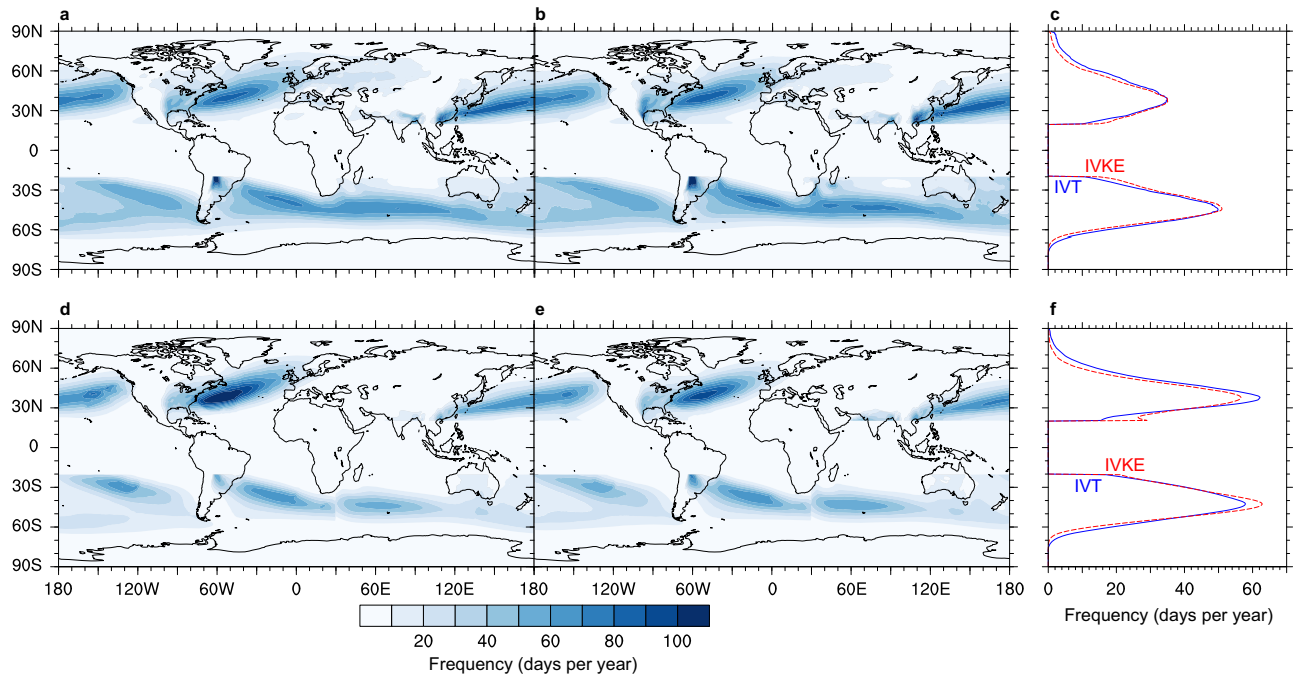

Fig. 1 | Atmospheric river (AR) frequency. The upper panels use the algorithm of TempestExtremes[24], and the lower panels use the algorithm of Mundhenk et al.[26]. **a**, **d** use the integrated vapor transport (IVT) to calculate the AR frequency, and **b**, **e** use the integrated vapor kinetic energy (IVKE) to calculate the AR frequency. **c**, **f** show zonally averaged results using IVT (blue solid) and IVKE (red dash). Source data are generated from MERRA-2 data (1980–2019) and are provided as a Source Data file.

($q^2\mathbf{u}\cdot\mathbf{F_T}$, including surface flux of momentum), and condensation of vapor ($2KqS_M$; MERRA-2 combines subgrid-scale moist convection, condensation, and evaporation of condensate into one variable, S_M[27]). PE conversion to KE can be interpreted as flowing down a slope of an isobaric surface ($-\mathbf{u}\cdot\nabla_p\Phi$)[28]. This term is absent from the CWV budget —widely used in earlier AR studies—but turns out to be of leading order importance in our following analysis. Latent heat release associated with vapor condensation cannot directly change VKE but may affect VKE through enhancing PE conversion to KE[29]. The other terms are negligible in our analysis (See Eq. (10) and Supplementary Table S1, where the analysis tendency introduced by the reanalysis[25] is included, and turbulence tendency of vapor includes surface flux of vapor[27]).

We make a regression-based AR composite and analyze its IVKE budget using MERRA-2 reanalysis data[25] from 2010 to 2019, a 10-year period sufficient to produce statistically significant results. Our composite AR is based on a widely used composite method to study extratropical cyclones[30], baroclinic waves[31,32], and convectively coupled circulations[33,34]. This analysis focuses on an active AR region in the North Pacific, where the IVKE temporal variance maximizes among regions that do not have tropical cyclones (Supplementary Fig. S1). We first calculate the time series of areal mean IVKE in the 1° × 1° box centered at 155°E 35°N and calculate its anomaly from the temporal mean. We then perform a regression analysis at each grid point: we regress anomalous fields of VKE, IVKE, and their tendency terms on the time series of IVKE anomaly that we just obtained. We multiply the regression coefficient of a given field at each grid point by one sample standard deviation of the IVKE time series to reconstruct the corresponding field of the composite AR. See Methods for more details about the regression-based composite.

This composite method, based on regression, provides an Eulerian perspective by focusing on the development of ARs passing through a specific area. It aligns with the current form of Eq. (3), suitable for assessing AR development, movement, and impact at a particular location. Alternatively, a Lagrangian approach constructs the composite by tracking and following AR events, offering insights into the evolution of VKE throughout the AR lifecycle. However, an AR-following reference frame that allows for diagnosing the underlying movement mechanisms is yet to be developed. In this paper, we focus on the Eulerian approach and plan to implement and present the AR-following perspective in a future study.

Through the lens of IVKE, the composite AR is an elongated ellipse with the major axis pointing toward the east-northeast (contours in Fig. 2). The total IVKE tendency leads the AR's IVKE anomaly by about a quarter cycle (Fig. 2a), suggesting that the total tendency makes little change to the IVKE amplitude but promotes the AR's eastward movement. We find that the horizonal VKE advection (Fig. 2b) has similar spatial structure and even overall amplitude to those of the total IVKE tendency (Fig. 2a). This result shows that the horizontal advection is the primary mechanism for the movement of ARs. We further decompose the horizontal advection of VKE into vapor and KE parts, and the vapor part leads to an eastward movement (Supplementary Fig. S2a) while the KE part may lead to an east-northeastward movement (Supplementary Fig. S2b). This result adds to earlier moisture budget analyses that only considered the role of horizontal advection of moisture.

The IVKE tendency due to PE conversion to KE is in phase with the AR's IVKE anomaly (Fig. 2c). Therefore, the energy conversion increases the AR's IVKE anomaly and is the primary process responsible for the AR's development and maintenance. IVKE tendency that lies outside of the AR's IVKE anomaly does not project onto the AR's IVKE anomaly and, thus, cannot affect the AR's intensity. This PE-to-KE conversion is essential to maintain the low-level jets[29], and this process was overlooked in earlier moisture budget analyses. We emphasize that the PE-to-KE conversion mainly arises from the anomalous winds that can have a significant ageostrophic component. For example, Supplementary Fig. S3a shows wind anomaly, geopotential, and specific humidity of the composite AR at 950 hPa, where VKE maximizes. There is a significant anomalous wind component that is directed across the geopotential gradient, converting PE to KE and accelerating the low-level jet (Supplementary Fig. S3a). On the other hand, the mean winds mainly follow the geopotential contours and contribute less to the PE-to-KE conversion (Supplementary Fig. S3b). We see similar patterns throughout pressure levels from 975 to 850 hPa (Supplementary Fig. S4 and Supplementary Video S2). For a further PE-to-KE conversion decomposition, see Supplementary Note, Equation S13, and Supplementary Fig. S13.

The vertical VKE advection also increases AR's IVKE anomaly near the center of the AR, where IVKE is large (Fig. 2d), so the vertical advection also contributes to the AR's development and maintenance. On the other hand, the AR loses KE through turbulent dissipation (Fig. 2e) and loses vapor through condensation (Fig. 2f). Both processes produce negative IVKE tendencies over the AR core and result in reductions of IVKE. Other physical processes make negligible contributions to the IVKE budget and show no values above the minimum contour level in Fig. 2. To test the robustness of our results, we make composite ARs in the AR active regions in the North Atlantic (Supplementary Fig. S5) and South Atlantic (Supplementary Fig. S6) and analyze their IVKE budget. The overall results remain similar. See Methods for more details about robustness testing.

Our analysis framework resolves the vertical dimension of the composite AR. Figure 3 shows an east-west vertical cross section through the center of the AR along 35°N. The VKE anomaly increases from the bottom to 950 hPa due to the strong low-level jet and high humidity. Then VKE decreases with altitude mainly due to the exponential decrease of water vapor (Fig. 3). The vertically resolved results supports the map view analysis (Fig. 2). The total VKE tendency promotes the AR's eastward movement (Fig. 3a). The horizonal VKE advection (Fig. 3b) shows a similar pattern and magnitude to the total VKE tendency (Fig. 3a). We also decompose the horizontal advection of VKE into vapor and KE parts (Supplementary Fig. S7a, b), and the results are consistent with the map view (Supplementary Fig. S2a, b). The PE conversion to KE is a source of VKE (Fig. 3c), and the turbulent dissipation of KE is a sink (Fig. 3e). The tendencies for both processes are concentrated between 1000 and 800 hPa. Condensation producing negative VKE tendencies over the AR core results in reductions of VKE and is distributed from 900 hPa to 500 hPa (Fig. 3f). The vertical VKE advection increases VKE above 950 hPa but decreases VKE from the surface to 950 hPa (Fig. 3d). Since the AR's VKE anomaly maximizes at 950 hPa, large-scale ascent in the AR advects VKE-rich air from lower altitude to higher above 950 hPa but the opposite below. When we decompose the vertical advection, the vapor part increases VKE (Supplementary Figs. S2c and S7c) while the KE part decreases VKE (Supplementary Figs. S2d and S7d) because specific humidity is maximized at lower levels, while KE is maximized at upper levels (Supplementary Video S2). Supplementary Fig. S8 shows a south-north vertical cross section through the center of the AR along 155°E. The AR's anomalous air motion is poleward and upward (Supplementary Fig. S8). The VKE contours above 950 hPa resemble a hill where the poleward slope is steeper than the equatorward slope (Supplementary Fig. S8). Such motion and asymmetry are consistent with findings of previous studies and are associated with the structure of the cold front[1,4,19].

We project each tendency term in Eq. (10) onto the regressed field of IVKE anomaly to quantify the contribution of the physical processes to the growth or decay of the composite AR (see Methods and Eq. (11a)). The projection value has a unit of inverse timescale and can be interpreted as a rate of growth or decay. We can also interpret this projection process as calculating the spatial correlation between a specific IVKE tendency term and the IVKE anomaly, given that the IVKE tendency terms can reinforce the IVKE anomaly or AR intensity only if

https://doi.org/10.1038/s41467-024-53369-0

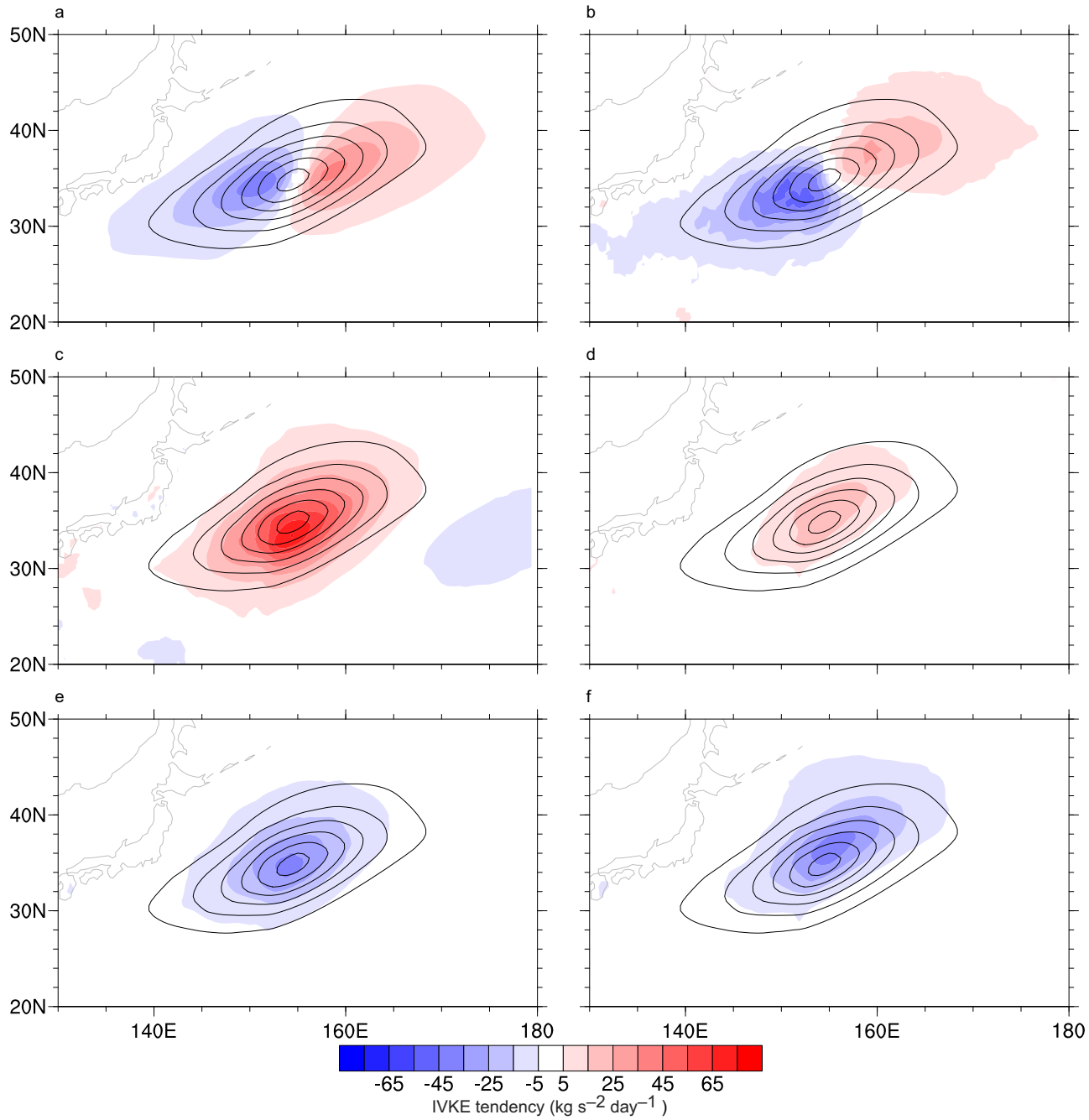

Fig. 2 | Plan view of the atmospheric river (AR) composite. The contours are the integrated vapor kinetic energy (IVKE) (interval: 5 kg s^{-2}). The shades are IVKE tendencies: **a** total tendency, **b** horizontal advection of vapor kinetic energy (VKE), **c** potential energy conversion to kinetic energy (KE), **d** vertical advection of VKE, **e** turbulent dissipation of KE, and **f** condensation of vapor. Source data are generated from MERRA-2 data (2010 to 2019) and are provided as a Source Data file.

they are in phase. On the other hand, if an IVKE tendency term has significant values outside the AR's IVKE anomaly, this physical process would not change the AR intensity. This quantitative analysis (Fig. 4a) agrees with our qualitative analysis (Fig. 2). The IVKE budget is well closed given a residual of only 0.6% of the sum of the IVKE sources (Supplementary Table S1).

We then measure the contribution to the AR's eastward movement by projecting each term on the right-hand side of Eq. (10) onto the total IVKE tendency of the composite AR (See Methods and Eq. (11b)). The horizontal VKE advection is the primary mechanism for the AR's eastward movement (Fig. 4b, d and Supplementary Table S1). We further show that the horizontal advection of vapor contributes more to the eastward movement than the horizontal advection of KE (Fig. 4b, d and Supplementary Table S1). Moving the boundary of the projection area does not affect the results unless doing so cuts off any contoured region of the AR's IVKE anomaly (Fig. 2) or shaded region of the AR's IVKE total tendency anomaly (Fig. 2a). The projection boundary cuts off a region of negative PE-to-KE conversion (Fig. 2c), but our calculations show that changing the cut does not affect the results, as the negative PE-to-KE region does not overlap with the area of significant AR's IVKE or its tendency.

To test the robustness of our composite and IVKE analysis, we perform identical calculations using an independent dataset, the ERA5 reanalysis data[35], from 2010 to 2019. The ERA5 results (Fig. 4c, d and Supplementary Fig. S9) agree well with the MERRA-2 results

https://doi.org/10.1038/s41467-024-53369-0

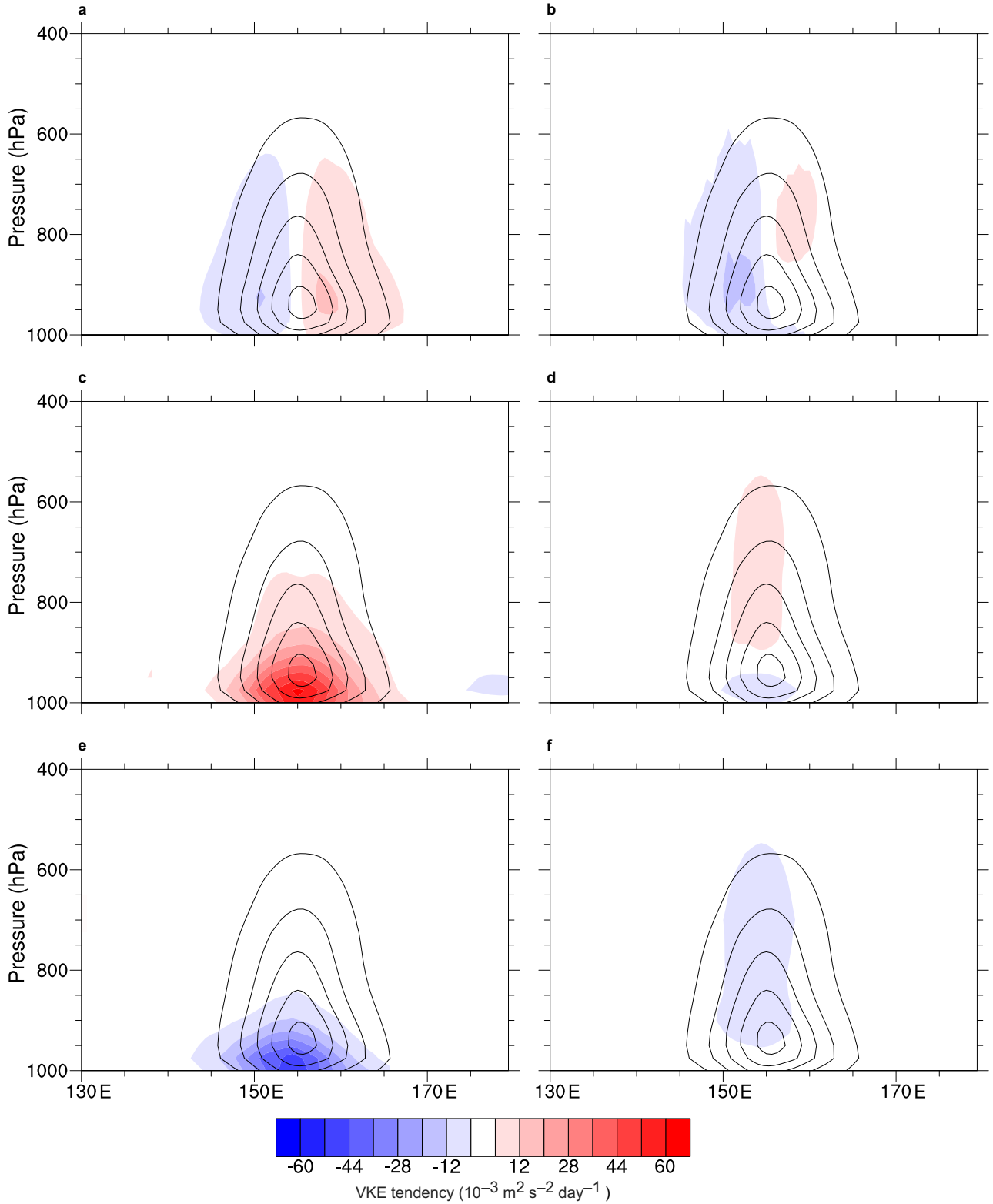

Fig. 3 | Vertical cross section of the atmospheric river (AR) composite averaged between 34.5°N and 35.5°N. The contours are vapor kinetic energy (VKE) (interval: 2×10^{-3} m^2 s^{-2}). The shades are VKE tendencies: **a** total tendency, **b** horizontal advection of VKE, **c** potential energy conversion to kinetic energy (KE), **d** vertical advection of VKE, **e** turbulent dissipation of KE, and **f** condensation of vapor. Source data are generated from MERRA-2 data (2010–2019) and are provided as a Source Data file.

(Figs. 2 and 4a, b). The minor discrepancies observed might be attributed to variations in the sampling frequency: ERA5 saves instantaneous data every hour, while MERRA-2 saves time-averaged data every 3 h. This agreement between the two datasets suggests that our analysis methods are reliable, and the emerging physics is robust regardless of the dataset employed.

The above analyses primarily focus on composite ARs at their peak intensity. What are the roles of different physical processes in

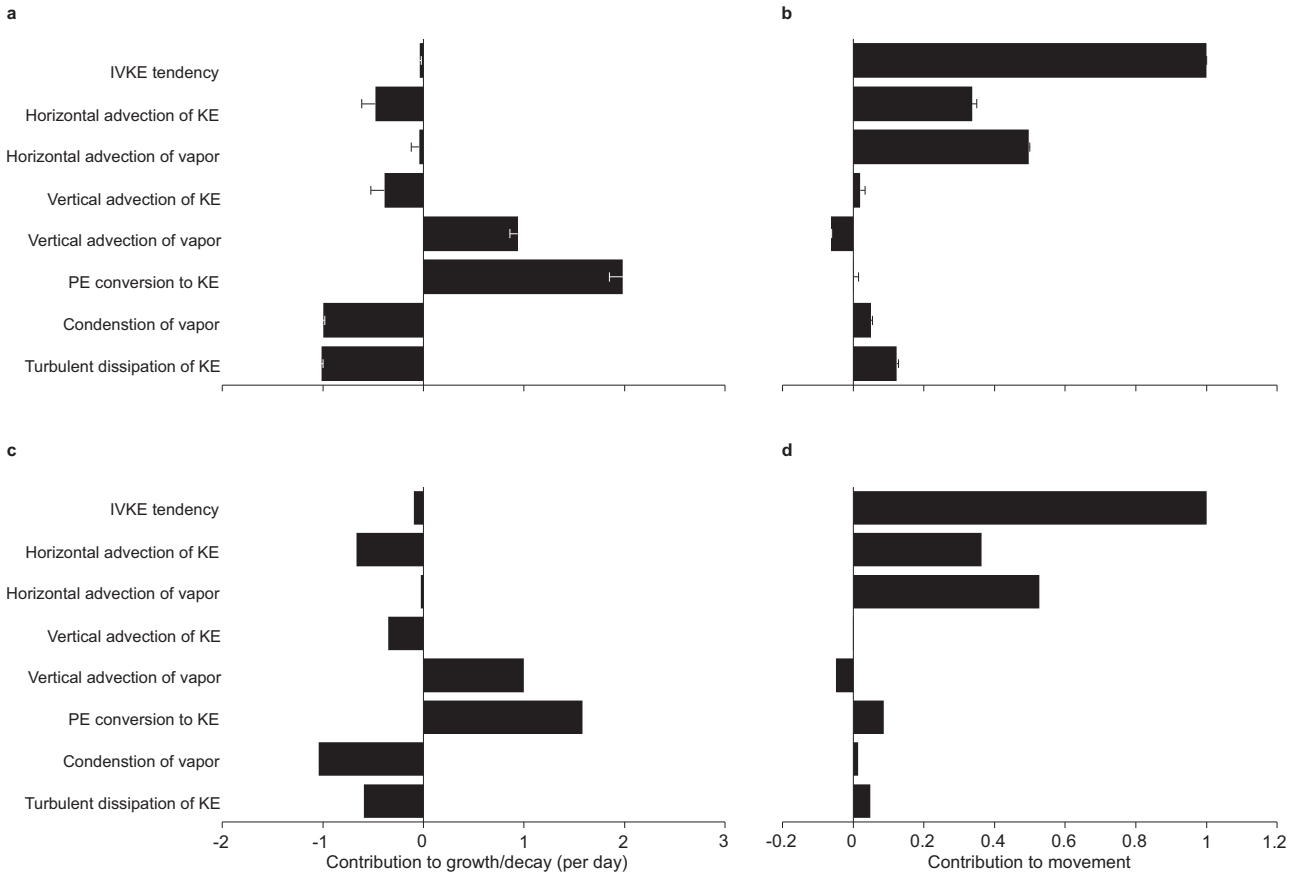

Fig. 4 | Budget analysis for the integrated vapor kinetic energy (IVKE). Contribution of physical processes to the growth or decay (**a**, **c**) and movement (**b**, **d**) of the composite atmospheric river (AR). **a**, **b** use MERRA-2 data, and **c**, **d** use ERA5 data within 130°E to 180°, 20°N to 50°N. In **a**, **b**, all the terms are directly calculated from MERRA-2 data, and the error bars represent the residuals (Supplementary Eqs. (S8)–(S10)). In **c**, **d**, condensation of vapor and turbulent dissipation of kinetic energy (KE) are not provided by ERA5 but are instead estimated from Supplementary Eqs. (S11) and (S12). See Supplementary Note for details. Source data are provided as a Source Data file.

different stages of ARs' lifecycles, including intensification and decay? We present a case study toward addressing this question. A historic AR made landfall onto the west coast of North America during 12 to 15 UTC, 4 January 2023 (Fig. 5a, b and Supplementary Video S3). This AR intensified before its landfall and decayed after its landfall. Supplementary Video S3 shows the 3-hourly evolution of this AR from 18 to 21 UTC, 3 January 2023 to 18 to 21 UTC, 4 January 2023. We take the projection of IVKE tendency (∂IVKE/∂t) on IVKE (Eq. (11a)) as the rate of growth (positive) or decay (negative); our projection region is 160°W to 100°W, 20°N to 50°N. The growth rate was 0.91 ± 0.02 day^{-1} from 18 to 21 UTC, 3 January 2023 (Fig. 5c), so the AR intensity changed by 12% within 3 hours. The AR intensity kept increasing by 10% in the next 3 h (Supplementary Video S3). Then, the AR maintained and slightly increased its intensity from 00 to 15 UTC, 4 January 2023 with a growth rate fluctuating from −0.04 to 0.40 day^{-1} (Supplementary Video S3). The AR decayed after landfall (Supplementary Video S3). The growth rate was -0.75 ± 0.01 day^{-1} from 18 to 21 UTC, 4 January 2023 (Fig. 5d), so the AR intensity changed by 9% within 3 hours. Throughout the AR evolution, the last four terms on our growth rate diagrams (Fig. 5c, d and Supplementary Video S3), including the contributions of PE-to-KE conversion, vertical advection of vapor, turbulent dissipation of KE, and condensation of vapor, remain as the most prominent terms, qualitatively similar to those in the composite AR (comparing Fig. 5c, d and Supplementary Video S3 to Fig. 4a, c). In addition, though the partition between the horizontal advection of KE and vapor changes throughout the AR lifecycle, their sum remains negative (Supplementary Video S3). In general, the IVKE sources are in excess during the growth stage, while the IVKE sinks are excessively negative during the decay stage (Fig. 5).

Discussion

Here we propose to use VKE to detect and study ARs, killing two birds with one stone (Table 1). IVKE is as effective as IVT in identifying and monitoring ARs. Additionally, the budget of IVKE distills fundamental AR physics: PE conversion to KE is the primary energy source to sustain ARs and is balanced by turbulent dissipation and condensation; horizontal advection of VKE leads to the eastward movement of ARs. Conversion from PE to KE is the main energy source for the low-level jet[29]. Therefore, our quantitative diagnosis of the IVKE budget confirms that the low-level jet is an integral part of ARs. This result complements prior observational studies that have documented the association between ARs and low-level jets[1,4]. Additionally, the advection of both vapor and KE contributes to ARs' eastward movement, indicating that both humidity and winds are important to ARs' evolution. This analysis framework complements earlier studies that focused on either ARs' humidity evolution or the role of extratropical cyclones in ARs' development, which puts AR research in a firmer footing in atmospheric dynamics.

One may think that analyzing the VKE budget is equivalent to analyzing the budgets of specific humidity and KE separately. However, that is not true. Due to stronger winds aloft, KE budget would emphasize much on the energetics in the upper troposphere, whereas lower-troposphere winds are most relevant to water vapor transport and thereby AR dynamics. VKE is the KE weighted by q^2. It shows a

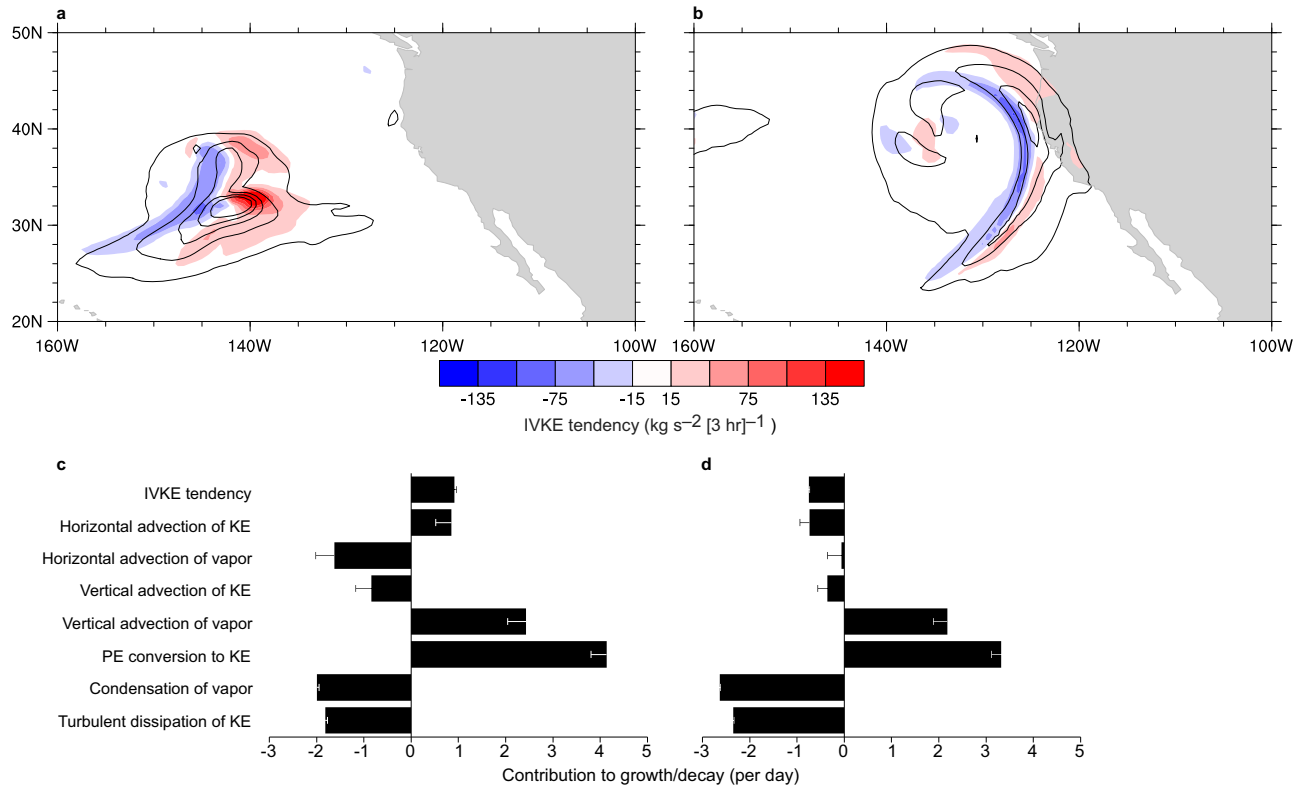

Fig. 5 | A case study of an atmospheric river (AR) event. a Temporal-mean integrated vapor kinetic energy (IVKE) (contours, minimum level: 15 kg s^{-2}, interval: 30 kg s^{-2}) and IVKE tendency (shading) during 18–21 UTC, 3 January 2023 (18 h before the AR landfall onto the west coast of North America, intensification stage). **c** IVKE budget analysis using temporal-mean data from this three-hour period, where the error bars represent the residuals (Supplementary Eqs. (S8)–(S10)). **b** and **d** are similar to **a** and **c** but for 18–21 UTC, 4 January 2023 (6 h after the AR landfall onto the west coast of North America, decaying stage). Source data are generated from MERRA-2 data and are provided as a Source Data file.

bottom-heavy structure and allows us to focus on the dynamics associated with low-level jets that effectively transport water vapor.

Unresolved physics, such as boundary layer turbulence and atmospheric convection, contribute substantially to the IVKE budget. This result suggests that although ARs span hundreds or even thousands of kilometers, accurately simulating and forecasting ARs require realistic representations of these sub-grid scale physical processes. Consequently, these processes should be key observation targets for future field campaigns.

What to do next? There is significant seasonal variability in the dynamics and frequency of ARs over the North Pacific. Our current composite analysis focuses on the entire time series of VKE. How might the results change if the budget analysis were conducted for individual seasons? Specifically, would the relative strength of the terms differ between winter and summer? ARs have different flavors and can occur at various locations, causing distinct extreme weather conditions. For example, ARs also occur in the eastern Pacific and often make landfall over the west coast of North America. Additionally, there are "windy" and "wet" ARs, producing different surface winds and precipitation[18]. Does the dominant balance of the VKE budget remain the same for all AR flavors at various locations? In this paper, we primarily focus on analyses of composite ARs that can be considered as a developed system. What are the roles of different physical processes in different stages of ARs' lifecycles, e.g., the generation, intensification, and decay? What leads to a windy AR versus a wet AR? ARs become weaker under the influence of industrial aerosols but become stronger with increasing greenhouse gases[36]. What leads to the distinct responses of ARs? Our IVKE framework provides a quantitative analysis framework to address these pressing questions that are key to preparing for AR-induced hydrologic extremes. In the future, we plan to implement AR-following composite method and diagnostic framework. This will allow us to investigate the VKE evolution throughout the AR lifecycle, complementing the Eulerian view presented in the current study.

Methods

Derivation of the IVKE budget

To derive the VKE prognostic equation, we start from the moisture prognostic equation:

$$\frac{\partial q}{\partial t} = -\mathbf{u}\cdot\nabla_p q - \omega\frac{\partial q}{\partial p} + S_{\mathrm{M}} + S_{\mathrm{T}} + S_{\mathrm{C}}, \tag{4}$$

and the hydrostatic primitive momentum prognostic equation:

$$\frac{\partial \mathbf{u}}{\partial t} = -\mathbf{u}\cdot\nabla_p \mathbf{u} - \omega\frac{\partial \mathbf{u}}{\partial p} - 2\Omega\sin\vartheta\,\mathbf{k}\times\mathbf{u} - \frac{u\tan\vartheta}{a}\mathbf{k}\times\mathbf{u} - \nabla_p\Phi + \mathbf{F_M} + \mathbf{F_T} + \mathbf{F_G}, \tag{5}$$

where the variables are defined as follows: $\mathbf{u}$, horizontal velocity vector; ω, vertical motion; Φ, geopotential; Ω, planetary rotation rate; a, planetary radius; ϑ, latitude. The variables $\mathbf{F_M}$, $\mathbf{F_T}$, and $\mathbf{F_G}$ denote apparent momentum sources or sinks due to subgrid-scale moist convection, turbulence, and gravity wave drag. The variables S_{M}, S_{T}, and S_{C} denote apparent moisture sources or sinks due to moist physics (including subgrid-scale moist convection, condensation, and evaporation of condensate, hereafter condensation), turbulence, and chemistry. In MERRA-2, tendencies due to dynamics refers to the combination of the first two terms on the right-hand side of Eq. (4) (hereafter, S_{D}) and the first five terms on that of Eq. (5) (hereafter, $\mathbf{F_D}$).

Table 1 | Comparison between the integrated vapor transport (IVT) and integrated vapor kinetic energy (IVKE) frameworks. Both frameworks can effectively track atmospheric rivers (ARs)

		IVT	IVKE
Tracking ARs using winds & moisture		**Yes**	**Yes**
Understanding	Governing equation	Unavailable	Eq. (3): ∂_tVKE = VKE advection + PE conversion to KE − KE dissipitation − condensation.
	Quantitative diagnosis for the development of ARs	Unavailable	Eq. (11a) & Figs. 2–5: Growth: PE conversion to KE and vertical advection of water vapor; Decay: Condensation of vapor and turbulent dissipation of KE.
	Quantitative diagnosis for the movement of ARs	Unavailable	Eq. (11b) & Figs. 2–4: Horizontal advection of KE and water vapor leads to the eastward movement of ARs.

The IVKE framework introduces a governing equation based on the conservation of energy and moisture, allowing quantitative diagnoses of the development and movement of ARs.

Then, we derive the prognostic equation of q^2 by multiplying 2q to Eq. (4) and applying the product rule ($2q\frac{\partial q}{\partial t}=\frac{\partial q^2}{\partial t}$):

$$\frac{\partial q^2}{\partial t}=-2q\mathbf{u}\cdot\boldsymbol{\nabla}_p q-2q\omega\frac{\partial q}{\partial p}+2qS_{\mathrm{M}}+2qS_{\mathrm{T}}+2qS_{\mathrm{C}}. \tag{6}$$

Additionally, we derive the prognostic equation of K by taking the dot product of $\mathbf{u}$ to Eq. (5) and applying the product rule ($\mathbf{u}\cdot\frac{\partial\mathbf{u}}{\partial t}=\frac{\partial}{\partial t}\left(\frac{\mathbf{u}\cdot\mathbf{u}}{2}\right)=\frac{\partial K}{\partial t}$; $-\mathbf{u}\cdot\left(\mathbf{u}\cdot\boldsymbol{\nabla}_p\mathbf{u}\right)=\mathbf{u}\cdot\boldsymbol{\nabla}_p\left(\frac{\mathbf{u}\cdot\mathbf{u}}{2}\right)=-\mathbf{u}\cdot\boldsymbol{\nabla}_p K$; $-\mathbf{u}\cdot\omega\frac{\partial\mathbf{u}}{\partial p}=-\omega\frac{\partial}{\partial p}\left(\frac{\mathbf{u}\cdot\mathbf{u}}{2}\right)=-\omega\frac{\partial K}{\partial p}$):

$$\frac{\partial K}{\partial t}=-\mathbf{u}\cdot\boldsymbol{\nabla}_p K-\omega\frac{\partial K}{\partial p}-\mathbf{u}\cdot\boldsymbol{\nabla}_p\Phi+\mathbf{u}\cdot\mathbf{F_M}+\mathbf{u}\cdot\mathbf{F_T}+\mathbf{u}\cdot\mathbf{F_G}, \tag{7}$$

Adding K times Eq. (6) and q^2 times Eq. (7) and applying the product rule ($K\frac{\partial q^2}{\partial t}+q^2\frac{\partial K}{\partial t}=\frac{\partial q^2 K}{\partial t}$) yields the VKE prognostic equation:

$$\begin{aligned}\frac{\partial q^2K}{\partial t}=&-q^2\mathbf{u}\cdot\boldsymbol{\nabla}_p K-q^2\omega\frac{\partial K}{\partial p}-q^2\mathbf{u}\cdot\boldsymbol{\nabla}_p\Phi+q^2\mathbf{u}\cdot\mathbf{F_M}+q^2\mathbf{u}\cdot\mathbf{F_T}\\&+q^2\mathbf{u}\cdot\mathbf{F_G}-2Kq\mathbf{u}\cdot\boldsymbol{\nabla}_p q-2Kq\omega\frac{\partial q}{\partial p}+2KqS_{\mathrm{M}}+2KqS_{\mathrm{T}}+2KqS_{\mathrm{C}}.\end{aligned} \tag{8}$$

Taking the time derivative of Eq. (2) and using the Leibniz integral rule yields a simple form of IVKE prognostic equation:

$$\frac{\partial}{\partial t}\langle q^2K\rangle=\left\langle\frac{\partial q^2K}{\partial t}\right\rangle+\left[\frac{q^2K}{g}\right]_{p_{\mathrm{B}}}\frac{\partial p_{\mathrm{B}}}{\partial t}, \tag{9}$$

where $\langle\,\rangle$ denotes the following integral operator:

$$\langle\rangle\equiv-\frac{1}{g}\int_{p_{\mathrm{B}}}^{p_{\mathrm{T}}}()\mathrm{d}p.$$

Plugging Eq. (8) into Eq. (9) yields the IVKE prognostic equation with complete physics:

$$\begin{aligned}\frac{\partial}{\partial t}\langle q^2K\rangle=&\underbrace{\left\langle-q^2\mathbf{u}\cdot\boldsymbol{\nabla}_p K\right\rangle}_{\mathrm{HAKE}}+\underbrace{\left\langle-q^2\omega\frac{\partial K}{\partial p}\right\rangle}_{\mathrm{VAKE}}+\underbrace{\left\langle-q^2\mathbf{u}\cdot\boldsymbol{\nabla}_p\Phi\right\rangle}_{\mathrm{PEKE}}+\underbrace{\langle q^2\mathbf{u}\cdot\mathbf{F_M}\rangle}_{\mathrm{MOKE}}\\&+\underbrace{\langle q^2\mathbf{u}\cdot\mathbf{F_T}\rangle}_{\mathrm{TOKE}}+\underbrace{\langle q^2\mathbf{u}\cdot\mathbf{F_G}\rangle}_{\mathrm{GOKE}}+\underbrace{\left\langle-2Kq\mathbf{u}\cdot\boldsymbol{\nabla}_p q\right\rangle}_{\mathrm{HAV}}+\underbrace{\left\langle-2Kq\omega\frac{\partial q}{\partial p}\right\rangle}_{\mathrm{VAV}}\\&+\underbrace{\langle 2KqS_{\mathrm{M}}\rangle}_{\mathrm{COV}}+\underbrace{\langle 2KqS_{\mathrm{T}}\rangle}_{\mathrm{TOV}}+\underbrace{\langle 2KqS_{\mathrm{C}}\rangle}_{\mathrm{CMOV}}+\underbrace{\left[\frac{q^2K}{g}\right]_{p_{\mathrm{B}}}\frac{\partial p_{\mathrm{B}}}{\partial t}}_{\mathrm{SPTE}}.\end{aligned} \tag{10}$$

The acronyms are defined as follows: horizontal advection of KE (HAKE), vertical advection of KE (VAKE), PE conversion to KE (PEKE), turbulent dissipation of KE (TOKE), moist convection tendency of KE (MOKE), gravity wave drag of KE (GOKE), horizontal advection of vapor (HAV), vertical advection of vapor (VAV), condensation of vapor (COV), turbulent tendency of vapor (TOV), chemistry tendency of vapor (CMOV), and surface pressure tendency effect (SPTE).

Moreover, the MERRA-2 provides nonphysical tendencies due to incorporating analysis data into winds ($\mathbf{F_A}$) and moisture (S_{A}), so we also calculate an analysis effect added to the right-hand side of Eq. (10) as $\langle q^2\mathbf{u}\cdot\mathbf{F_A}+2KqS_{\mathrm{A}}\rangle$. For a further PE-to-KE conversion decomposition, see Supplementary Note, Supplementary Eq. (S13), and Supplementary Fig. (S13).

Numerical analyses of IVT, VKE, IVKE, and tendency terms

We calculate IVT, VKE, IVKE, and all tendency terms (all terms in Eqs. (8) and (10)) from the MERRA-2 data[25]. To calculate IVT, VKE and its tendency, IVKE and its tendency, and surface pressure tendency effect, we take the p_{B}, q, and $\mathbf{u}$ from the 3-dimensional, 3-hourly, instantaneous, pressure-level, assimilated meteorological fields (inst3_3d_asm_Np in MERRA-2)[37] from 1980 to 2019. We use the Boer scheme[38,39] for the vertical integration and use forward differencing for VKE and IVKE tendencies and surface pressure tendency effect. Note that the instantaneous time steps and the tendency time steps are staggered intentionally, as the (3-hourly averaged) tendency is the time rate of change between two instantaneous time steps. In addition, taking the Φ, ω, p_{B}, q, and $\mathbf{u}$ from the 3-dimensional, 3-hourly, time-averaged, model-level, assimilated meteorological fields (tavg3_3d_asm_Nv[40]) from 2010 to 2019, we linearly interpolate them from the model levels to the pressure levels and calculate VKE and IVKE tendencies due to PE conversion to KE and horizontal and vertical advection of both KE and vapor using central differencing in space. We also calculate the abovementioned terms from the ERA5 global reanalysis[35] from 2010 to 2019, which are 3-dimensional, 1-hourly, instantaneous, pressure-level, assimilated meteorological fields. To calculate all the other tendency terms, we further take the corresponding time-averaged wind tendencies (all variables in tavg3_3d_udt_Np in MERRA-2)[41] and moisture tendencies (all variables starting with "DQVDT" in tavg3_3d_qdt_Np in MERRA-2)[42] from 2010 to 2019. In the wind tendency data, horizontal advection, vertical advection, Coriolis effect, curvature effect, and geopotential gradient are combined into a tendency of winds due to dynamics. Also, in the moisture tendency data, horizontal advection and vertical advection are combined into a tendency of specific humidity due to dynamics. We take these wind and moisture tendencies due to dynamics to calculate VKE and IVKE tendencies due to dynamic tendency of KE and vapor. We denote any given term on the right-hand side of Eq. (10) as X. Then, following Anderson and Kuang's[33] method and notation (|| || denotes surface integral), we estimate X's contribution to AR's growth and movement by projecting X onto IVKE and total IVKE tendency (∂_tIVKE):

$$\text{contribution to growth or decay}=||X(IVKE)||/||(IVKE)^2||,\text{ and} \tag{11a}$$

$$\text{contribution to movement}=||X\partial_t IVKE||/||(\partial_t IVKE)^2||. \tag{11b}$$

AR detection and frequency

We detect ARs with two algorithms. First, we use the TempestExtremes[24] algorithm with thresholds following McClenny, Ullrich, and Grotjahn[43] except following Rhoades et al.[44] for omitting the additional threshold filtering out tropical cyclones. This method features the Laplacian of IVT <−40,000 kg m^{-1} s^{-1} rad^{-2}. For comparison, we test this method with the Laplacian of IVKE instead of IVT with various threshold values. Among the threshold values, we select the Laplacian of IVKE <−2000 kg s^{-2} rad^{-2}, which best reproduces the globally averaged AR frequency using IVT with the above threshold (IVT <−40,000 kg m^{-1} s^{-1} rad^{-2}); the AR frequency is the ratio of time steps with AR presence to total time steps. All other thresholds remain the same, including the exclusion of grid points between 20°S and 20°N and the exclusion of blobs with less than 50 connected grid points.

We also detect ARs using the algorithm by Mundhenk, Barnes, and Maloney[26]. This method uses the following thresholds: minimum IVT = 250 kg m^{-1} s^{-1}, minimum blob size = 150 contiguous grid points, minimum length-width ratio = 1.6, minimum orientation off the parallel = 0.95 rad, minimum length = 25 grid points, minimum mean IVT anomaly = 305 kg m^{-1} s^{-1}, and minimum eccentricity = 0.87. We exclude grid points between 20°S and 20°N. When switching to IVKE, we test various minimum IVKE and minimum mean IVKE anomaly and find the combination that best reproduces the globally averaged AR frequency using Mundhenk, Barnes, and Maloney's thresholds. Optimal results are found when the minimum IVKE = 14 kg s^{-2} and the minimum mean IVKE anomaly = 20 kg s^{-2}. We use MERRA-2 data from 1980 to 2019 for both algorithms.

AR composite and IVKE budget analysis

We design an AR composite based on IVKE temporal variance independently from any AR detection method. Here we use data from 2010 to 2019. We sought the IVKE standard deviation map (Supplementary Fig. S1) for local maxima of IVKE variance without overlapping with tropical cyclone tracks[45]. We select three spatial maxima of IVKE variance at 155°E 35°N (North Pacific), 60°W 40°N (North Atlantic), and 27.5°W 37.5°S (South Atlantic). The corresponding plotting and projecting regions are 130°E to 180°, 20°N to 50°N (North Pacific), 85°W to 35°W, 25°N to 55°N (North Atlantic), and 52.5°W to 2.5°W, 52.5°S to 22.5°S (South Atlantic). We confirm that there is high AR frequency at the selected points (Fig. 1) and no tropical cyclone track within 2° around the selected points from 2010 to 2019[45]. We take the time series of spatial averaged IVKE in the 1° × 1° box centered at the selected points as an AR index (e.g., Supplementary Fig. S10). Also, we removed the temporal mean from the fields of the VKE, IVKE, and all the tendency terms as anomalies. Then, we regress the anomaly at each grid point upon the AR index and multiply the regression coefficient at each grid point by one sample standard deviation of the AR index. This calculation yields the composite AR. We test the robustness of our composite results by switching between MERRA-2 and ERA5 data. Additionally, we excluded the time steps when AR is not detected in the 1° × 1° box, e.g., centered at 155°E 35°N using the TempestExtremes as described in Methods, and the results remain similar (Comparing Fig. 2 to Supplementary Fig. S11). All shown regressed fields are significant at 95% confidence level at each grid point with the two-tailed Student's *t*-test, where the degrees of freedom account for lag autocorrelation[39,46]. The statistically insignificant data points are small valued, so we color them in white in the figures. We analyze IVKE budget of the composite AR by projection as described in Methods. We test the robustness of our projection results by varying the boundary of our composite domain, and the results remain similar as long as the boundary does not cut off any composite AR signal (Comparing Fig. 4a, b to Supplementary Fig. S12).

Data availability

The MERRA-2 data used in this study are available in Goddard Earth Sciences Data and Information Services Center (GES DISC) at https://doi.org/10.5067/QBZ6MG944HW0[37], https://doi.org/10.5067/SUOQESM06LPK[40], https://doi.org/10.5067/CWV0G3PPPWFW[41], and https://doi.org/10.5067/A9KWADY78YHQ[42]. The ERA5 data used in this study are available in Research Data Archive at the National Center for Atmospheric Research at https://doi.org/10.5065/BH6N-5N20[47]. The tropical cyclone track used in this study aiding the AR regression region selection are visualized at https://coast.noaa.gov/hurricanes/ while the data are available in NOAA National Centers for Environmental Information at https://doi.org/10.25921/82ty-9e16[48]. The data generated for Figs. 1–5 are provided in the Source Data file. Source data are provided with this paper.

Code availability

The TempestExtremes version 2.2.1 algorithm for the AR detection is available in GitHub at https://github.com/ClimateGlobalChange/tempestextremes[49]. The AR detection algorithm of Mundhenk, Barnes, and Maloney is available in Digital Collections of Colorado at http://hdl.handle.net/10217/170619. The NCAR Command Language (NCL) version 6.6.2 built-in functions for the numerical analyses are available at https://doi.org/10.5065/D6WD3XH5[39]. Custom scripts for applying NCL and TempestExtremes are available at https://doi.org/10.5281/zenodo.13883900[50].

References

1. Ralph, F. M., Dettinger, M. D., Cairns, M. M., Galarneau, T. J. & Eylander, J. Defining "atmospheric river": How the Glossary of Meteorology helped resolve a debate. *Bull. Am. Meteorological Soc.* **99**, 837–839 (2018).
2. Guo, Y., Shinoda, T., Guan, B., Waliser, D. E. & Chang, E. K. Statistical relationship between atmospheric rivers and extratropical cyclones and anticyclones. *J. Clim.* **33**, 7817–7834 (2020).
3. Zhang, Z., Ralph, F. M. & Zheng, M. The relationship between extratropical cyclone strength and atmospheric river intensity and position. *Geophys. Res. Lett.* **46**, 1814–1823 (2019).
4. Ralph, F. et al. Dropsonde observations of total integrated water vapor transport within North Pacific atmospheric rivers. *J. Hydrometeorol.* **18**, 2577–2596 (2017).
5. Zhu, Y. & Newell, R. E. A proposed algorithm for moisture fluxes from atmospheric rivers. *Monthly Weather Rev.* **126**, 725–735 (1998).
6. Rutz, J. J. et al. The atmospheric river tracking method intercomparison project (ARTMIP): quantifying uncertainties in atmospheric river climatology. *J. Geophys. Res. Atmos.* **124**, 13777–13802 (2019).
7. Waliser, D. & Guan, B. Extreme winds and precipitation during landfall of atmospheric rivers. *Nat. Geosci.* **10**, 179–183 (2017).
8. Blamey, R., Ramos, A., Trigo, R., Tomé, R. & Reason, C. The influence of atmospheric rivers over the South Atlantic on winter rainfall in South Africa. *J. Hydrometeorol.* **19**, 127–142 (2018).
9. Kamae, Y., Mei, W. & Xie, S.-P. Climatological relationship between warm season atmospheric rivers and heavy rainfall over East Asia. *J. Meteorological Soc. Jpn. Ser. II* **95**, 411–431 (2017).
10. Kingston, D. G., Lavers, D. A. & Hannah, D. M. Floods in the Southern Alps of New Zealand: The importance of atmospheric rivers. *Hydrological Process.* **30**, 5063–5070 (2016).
11. Lavers, D. A. & Villarini, G. The nexus between atmospheric rivers and extreme precipitation across Europe. *Geophys. Res. Lett.* **40**, 3259–3264 (2013).
12. Neiman, P. J., Ralph, F. M., Wick, G. A., Lundquist, J. D. & Dettinger, M. D. Meteorological characteristics and overland precipitation impacts of atmospheric rivers affecting the West Coast of North America based on eight years of SSM/I satellite observations. *J. Hydrometeorol.* **9**, 22–47 (2008).

13. Viale, M., Valenzuela, R., Garreaud, R. D. & Ralph, F. M. Impacts of atmospheric rivers on precipitation in southern South America. *J. Hydrometeorol.* **19**, 1671–1687 (2018).
14. King, D. & Mehle, M. *Overview - Atmospheric River - October 24-25, 2021 Early Season Storm Brought Historic Heavy Rains and Strong Winds to the Bay Area*. National Weather Service. https://www.weather.gov/mtr/AtmosphericRiver_10_24-25_2021 [Accessed 31 October 2022] (2021).
15. Ralph, F. M. et al. Atmospheric rivers emerge as a global science and applications focus. *Bull. Am. Meteorological Soc.* **98**, 1969–1973 (2017).
16. Shields, C. A. et al. Atmospheric river tracking method intercomparison project (ARTMIP): project goals and experimental design. *Geosci. Model Dev.* **11**, 2455–2474 (2018).
17. Lora, J. M., Shields, C. & Rutz, J. Consensus and disagreement in atmospheric river detection: ARTMIP global catalogues. *Geophys. Res. Lett.* **47**, e2020GL089302 (2020).
18. Gonzales, K. R., Swain, D. L., Barnes, E. A. & Diffenbaugh, N. S. Moisture-versus wind-dominated flavors of atmospheric rivers. *Geophys. Res. Lett.* **47**, e2020GL090042 (2020).
19. Cordeira, J. M., Ralph, F. M. & Moore, B. J. The development and evolution of two atmospheric rivers in proximity to western North Pacific tropical cyclones in October 2010. *Monthly Weather Rev.* **141**, 4234–4255 (2013).
20. Dacre, H. F., Clark, P. A., Martinez-Alvarado, O., Stringer, M. A. & Lavers, D. A. How do atmospheric rivers form? *Bull. Am. Meteorological Soc.* **96**, 1243–1255 (2015).
21. Guan, B., Waliser, D. E. & Ralph, F. M. A multimodel evaluation of the water vapor budget in atmospheric rivers. *Ann. N. Y. Acad. Sci.* **1472**, 139–154 (2020).
22. Norris, J. R. et al. The observed water vapor budget in an atmospheric river over the northeast Pacific. *J. Hydrometeorol.* **21**, 2655–2673 (2020).
23. Lu, J. et al. Enhanced hydrological extremes in the western United States under global warming through the lens of water vapor wave activity. *npj Clim. Atmos. Sci.* **1**, 1–9 (2018).
24. Ullrich, P. A. et al. TempestExtremes v2.1: a community framework for feature detection, tracking, and analysis in large datasets. *Geosci. Model Dev.* **14**, 5023–5048 (2021).
25. Gelaro, R. et al. The modern-era retrospective analysis for research and applications, version 2 (MERRA-2). *J. Clim.* **30**, 5419–5454 (2017).
26. Mundhenk, B. D., Barnes, E. A. & Maloney, E. D. All-season climatology and variability of atmospheric river frequencies over the North Pacific. *J. Clim.* **29**, 4885–4903 (2016).
27. Molod, A., Takacs, L., Suarez, M. & Bacmeister, J. Development of the GEOS-5 atmospheric general circulation model: Evolution from MERRA to MERRA2. *Geosci. Model Dev.* **8**, 1339–1356 (2015).
28. Vincent, D. & Chang, L. Some further considerations concerning energy budgets of moving systems. *Tellus* **25**, 224–232 (1973).
29. Chen, X. A. & Chen, Y.-L. Kinetic energy budgets of the low-level jet during TAMEX IOP 5. *J. Meteorological Soc. Jpn. Ser. II* **80**, 1–19 (2002).
30. Lehmann, J. & Coumou, D. The influence of mid-latitude storm tracks on hot, cold, dry and wet extremes. *Sci. Rep.* **5**, 17491 (2015).
31. Chang, E. K. Downstream development of baroclinic waves as inferred from regression analysis. *J. Atmos. Sci.* **50**, 2038–2053 (1993).
32. Lim, G. H. & Wallace, J. M. Structure and evolution of baroclinic waves as inferred from regression analysis. *J. Atmos. Sci.* **48**, 1718–1732 (1991).
33. Andersen, J. A. & Kuang, Z. Moist static energy budget of MJO-like disturbances in the atmosphere of a zonally symmetric aquaplanet. *J. Clim.* **25**, 2782–2804 (2012).
34. Zhang, C. & Ling, J. Potential vorticity of the Madden–Julian oscillation. *J. Atmos. Sci.* **69**, 65–78 (2012).
35. Hersbach, H. et al. The ERA5 global reanalysis. *Q. J. R. Meteorological Soc.* **146**, 1999–2049 (2020).
36. Baek, S. H. & Lora, J. M. Counterbalancing influences of aerosols and greenhouse gases on atmospheric rivers. *Nat. Clim. Change* **11**, 958–965 (2021).
37. Global Modeling and Assimilation Office (GMAO). *MERRA-2 inst3_3d_asm_Np: 3d, 3-Hourly, Instantaneous, Pressure-Level, Assimilation, Assimilated Meteorological Fields V5.12.4* https://doi.org/10.5067/QBZ6MG944HW0 (Goddard Earth Sciences Data and Information Services Center (GES DISC), 2015).
38. Boer, G. J. Diagnostic equations in isobaric coordinates. *Monthly Weather Rev.* **110**, 1801–1820 (1982).
39. National Center for Atmospheric Research (NCAR). *The NCAR Command Language (Version 6.6.2)* https://doi.org/10.5065/D6WD3XH5 (2018).
40. Global Modeling and Assimilation Office (GMAO). MERRA-2 tavg3_3d_asm_Nv: 3d, 3-Hourly, Time-Averaged, Model-Level, Assimilation, *Assimilated Meteorological Fields V5.12.4* https://doi.org/10.5067/SUOQESM06LPK (Goddard Earth Sciences Data and Information Services Center (GES DISC), 2015).
41. Global Modeling and Assimilation Office (GMAO). *MERRA-2 tavg3_3d_udt_Np: 3d, 3-Hourly, Time-Averaged, Pressure-Level, Assimilation, Wind Tendencies V5.12.4* https://doi.org/10.5067/CWV0G3PPPWFW (Goddard Earth Sciences Data and Information Services Center (GES DISC), 2015).
42. Global Modeling and Assimilation Office (GMAO). *MERRA-2 tavg3_3d_qdt_Np: 3d, 3-Hourly, Time-Averaged, Pressure-Level, Assimilation, Moist Tendencies V5.12.4* https://doi.org/10.5067/A9KWADY78YHQ (Goddard Earth Sciences Data and Information Services Center (GES DISC), 2015).
43. McClenny, E. E., Ullrich, P. A. & Grotjahn, R. Sensitivity of atmospheric river vapor transport and precipitation to uniform sea surface temperature increases. *J. Geophys. Res. Atmos.* **125**, e2020JD033421 (2020).
44. Rhoades, A. M. et al. Influences of North Pacific Ocean domain extent on the western US winter hydroclimatology in variable-resolution CESM. *J. Geophys. Res. Atmos.* **125**, e2019JD031977 (2020).
45. Knapp, K. R., Kruk, M. C., Levinson, D. H., Diamond, H. J. & Neumann, C. J. The international best track archive for climate stewardship (IBTrACS) unifying tropical cyclone data. *Bull. Am. Meteorological Soc.* **91**, 363–376 (2010).
46. Zwiers, F. W. & Von Storch, H. Taking serial correlation into account in tests of the mean. *J. Clim.* **8**, 336–351 (1995).
47. European Centre for Medium Range Weather Forecasts. *ERA5 Reanalysis (0.25 Degree Latitude-Longitude Grid)* https://doi.org/10.5065/BH6N-5N20 (Research Data Archive at the National Center for Atmospheric Research, Computational and Information Systems Laboratory, 2019).
48. Knapp, K. R., Diamond, H. J., Kossin, J. P., Kruk, M. C. & Schreck, C. *International best track archive for climate stewardship (IBTrACS) project, version 4* https://doi.org/10.25921/82ty-9e16 (NOAA National Centers for Environmental Information, 2018).
49. Ullrich, P. *ClimateGlobalChange/tempestextremes (Version 2.2.1)*. https://github.com/ClimateGlobalChange/tempestextremes [Accessed 21 February 2023] (2022).
50. Ong, H. & Yang, D. Codes for "Vapor Kinetic Energy for the Detection and Understanding of Atmospheric Rivers". *Zenodo* https://doi.org/10.5281/zenodo.13883900 (2024).

Acknowledgements

This research is supported by a Packard Fellowship awarded to D.Y. This work was performed when H.O. was a postdoctoral scholar in D.Y.'s

group. We would like to acknowledge computing support from the Casper system (https://ncar.pub/casper) provided by the NSF National Center for Atmospheric Research (NCAR), sponsored by the National Science Foundation. We thank Paul Ullrich for the technical support on the use of TempestExtremes algorithm.

Author contributions

D.Y. designed and oversaw the research. H.O. performed the research. H.O and D.Y. wrote the paper together.

Competing interests

The authors declare no competing interests.

Additional information

Supplementary information The online version contains supplementary material available at https://doi.org/10.1038/s41467-024-53369-0.

Correspondence and requests for materials should be addressed to Da Yang.

Peer review information *Nature Communications* thanks the anonymous reviewers for their contribution to the peer review of this work. A peer review file is available.

Reprints and permissions information is available at http://www.nature.com/reprints

Publisher's note Springer Nature remains neutral with regard to jurisdictional claims in published maps and institutional affiliations.

Open Access This article is licensed under a Creative Commons Attribution-NonCommercial-NoDerivatives 4.0 International License, which permits any non-commercial use, sharing, distribution and reproduction in any medium or format, as long as you give appropriate credit to the original author(s) and the source, provide a link to the Creative Commons licence, and indicate if you modified the licensed material. You do not have permission under this licence to share adapted material derived from this article or parts of it. The images or other third party material in this article are included in the article's Creative Commons licence, unless indicated otherwise in a credit line to the material. If material is not included in the article's Creative Commons licence and your intended use is not permitted by statutory regulation or exceeds the permitted use, you will need to obtain permission directly from the copyright holder. To view a copy of this licence, visit http://creativecommons.org/licenses/by-nc-nd/4.0/.

© The Author(s) 2024